PNAS RESEARCH ARTICLE | PLANT BIOLOGY

Structures and organizations of PSI–AcpPCI supercomplexes from red tidal and coral symbiotic photosynthetic dinoflagellates

Xiaoyi Li[a,1], Zhenhua Li[a,b,1], Fangfang Wang[c,1], Songhao Zhao[a,b], Caizhe Xu[a,d], Zhiyuan Mao[a,b], Jialin Duan[c], Yue Feng[a,b], Yang Yang[a,e], Lili Shen[a,b], Guanglei Wang[a,b], Yanyan Yang[a], Long-Jiang Yu[a,f], Min Sang[f], Guangye Han[a,f], Xuchu Wang[e,g], Tingyun Kuang[a,f], Jian-Ren Shen[a,f,h], and Wenda Wang[a,f,2]

Edited by Donald Ort, University of Illinois at Urbana Champaign, Urbana, IL; received September 7, 2023; accepted January 2, 2024

Marine photosynthetic dinoflagellates are a group of successful phytoplankton that can form red tides in the ocean and also symbiosis with corals. These features are closely related to the photosynthetic properties of dinoflagellates. We report here three structures of photosystem I (PSI)–chlorophylls (Chls) *a*/*c*-peridinin protein complex (PSI–AcpPCI) from two species of dinoflagellates by single-particle cryoelectron microscopy. The crucial PsaA/B subunits of a red tidal dinoflagellate *Amphidinium carterae* are remarkably smaller and hence losing over 20 pigment-binding sites, whereas its PsaD/F/I/J/L/M/R subunits are larger and coordinate some additional pigment sites compared to other eukaryotic photosynthetic organisms, which may compensate for the smaller PsaA/B subunits. Similar modifications are observed in a coral symbiotic dinoflagellate *Symbiodinium* species, where two additional core proteins and fewer AcpPCIs are identified in the PSI–AcpPCI supercomplex. The antenna proteins AcpPCIs in dinoflagellates developed some loops and pigment sites as a result to accommodate the changed PSI core, therefore the structures of PSI–AcpPCI supercomplex of dinoflagellates reveal an unusual protein assembly pattern. A huge pigment network comprising Chls *a* and *c* and various carotenoids is revealed from the structural analysis, which provides the basis for our deeper understanding of the energy transfer and dissipation within the PSI–AcpPCI supercomplex, as well as the evolution of photosynthetic organisms.

dinoflagellates | photosynthesis | cryoelectron microscopy | photosystem I | light-harvesting antennae

Significance

Photosystem I (PSI) is an efficient photosynthetic supercomplex comprising peripheral antennae and core subunits. During evolution from cyanobacteria to plants, structures of the PSI core are highly conserved, whereas its light-harvesting complexes are varied. We resolved three PSI–AcpPCI structures from two dinoflagellates by cryo-EM, revealing unprecedented changes in the major and minor PSI core subunits. The major PsaA/B subunits are notably smaller and lack more than 20 pigments, whereas PsaD/F/I/J/L/M/R are larger. Their antennae share homologues with those in red algae and diatoms, which are properly assembled with the altered PSI core and organized as an efficient energy transfer network. These results reveal that dinoflagellate PSI–AcpPCI originates from red algae and develops specific characteristics during secondary endosymbiosis.

Oxygenic photosynthetic organisms play a crucial role in maintaining most lives on the earth by providing oxygen and energy. Photosystem I (PSI) and photosystem II (PSII) are two large membrane-embedded pigment-protein supercomplexes located in the thylakoid membranes that perform the initial processes of photochemical energy conversion (1), among which PSI is primarily responsible for harvesting light and generating electrons to reduce $NADP^+$ (2). Through the long years of evolutionary history from prokaryotic cyanobacteria to modern higher plants and algae, PSI has exhibited relatively conserved core structures and associated cofactors (3, 4), among which, the PsaA/B/C/D/E/F/I/J/L subunits of PSI are retained to fulfill photochemical and assemble functions. On the other hand, other minor Psa subunits, especially the peripheral light-harvesting complexes (LHCs), exhibit large variations among different organisms (3, 4).

Eukaryotic photosynthetic organisms have developed various numbers and types of LHC antennae, which interact with the PSI core and combine a large number of pigments to utilize different wavelengths of light in order to adapt to varying light environments (3, 4). The Lhca-type antennae in green algae and higher plants bind Chls *a*, Chls *b*, and several carotenoids (Cars), and comprise 4–10 Lhca subunits in each PSI core, forming the PSI–LHCI supercomplexes (5–13). The isolated red algal PSI of *Cyanidioschyzon merolae* have either 3 or 5 Lhcr-type antennae, containing Chls *a* and zeaxanthins as light-harvesting pigments (14, 15). Moreover, many "red" eukaryotic organisms arose from secondary endosymbiosis of red algae, such as diatoms and cryptophytes, have evolved numerous Lhcr or Lhcf antennae associated with PSI (16–22). LHC antennae of diatoms bind Chls *a*, Chls *c*, and keto-Car (fucoxanthin, Fx) and xanthophyll cycle (diadinoxanthin, Ddx; diatoxanthin, Dtx) (17, 18, 22). These Chls *c* and specific Cars can harvest more blue-green light and participate in the one-step deepoxidation/epoxidation cycle, improving the ability of diatoms to utilize more blue-green light available under water and to acclimate to the fluctuations of light in the aquatic environments (23–25).

Marine dinoflagellates are an important group of planktonic photosynthetic organisms that mainly stem from red algae via endosymbiosis and play a significant contribution to global primary productivity similar to diatoms (26–28). Marine dinoflagellates prosper under relatively quiescent water conditions and achieved remarkable ecological successes,

Author contributions: J.-R.S. and W.W. designed research; X.L., Z.L., and F.W. performed research; X.L., Z.L., F.W., S.Z., C.X., Z.M., J.D., Y.F., Yang Yang, L.S., G.W., Yanyan Yang, L.-J.Y., M.S., G.H., X.W., T.K., J.-R.S., and W.W. analyzed data; and X.L., Z.L., J.-R.S., and W.W. wrote the paper.

The authors declare no competing interest.

This article is a PNAS Direct Submission.

[1]X.L., Z.L., and F.W. contributed equally to this work.

[2]To whom correspondence may be addressed. Email: wdwang@ibcas.ac.cn.

This article contains supporting information online at https://www.pnas.org/lookup/suppl/doi:10.1073/pnas.2315476121/-/DCSupplemental.

Published February 6, 2024.

such as the formation of red tides and symbiosis with coral (29, 30). Most Photosynthetic dinoflagellates possess Chls *a*, Chls *c*, Ddx/Dtx, and another keto-Car called peridinin (Per), analogous to those found in diatoms (31–34). In addition to the membrane-spanning Chls *a*/*c*-peridinin protein complex (AcpPC) associated with PSI and PSII (31–34), dinoflagellates have developed a unique water-soluble peridinin-chlorophyll-protein (PCP) as their antenna. This antenna binds 8 Pers and 2 Chls *a*, forming two pigment clusters within each monomer, which efficiently harvest more blue-green light (470 to 550 nm) (34) than the typical Chl *a*/*b* binding antennae in green algae and higher plants. Therefore, PS supercomplexes and associated PCP or AcpPC antennae of dinoflagellates contribute to enhancing their photosynthetic efficiency, enabling them to flourish in marine red tide or provide support to form symbiosis within the host corals.

Despite the great ecological success of dinoflagellates, little is known about the structures of their PS supercomplexes involving the core and antenna subunits, therefore the arrangement of proteins and pigments for efficient light conversion are largely unknown. In this study, we determined a PSI–AcpPCI structure of *Amphidinium carterae* (Ac) and two PSI–AcpPCI structures of *Symbiodinium* species (Ss) by single-particle cryoelectron microscopy (cryo-EM). These three PSI–AcpPCI structures reveal the specific features of the dinoflagellate PSI core and accessory light-harvesting antennae, providing a solid structural basis for understanding the mechanisms of protein assembly and light harvesting within the dinoflagellate PSI–AcpPCI supercomplex.

Results

Overall Structure. Two PSI–AcpPCI samples were isolated from *A. carterae* and *Symbiodinium* species cells, a typical red tidal dinoflagellate and a coral symbiotic dinoflagellate (may be a mixture of several *Symbiodinium* species), respectively. The PSI–AcpPCI supercomplexes of *A. carterae* (Ac-PSI–AcpPCI) and *Symbiodinium* species (Ss-PSI–AcpPCI) were identified as the main brown-green bands separated in the sucrose density gradient through analyses of SDS-PAGE and mass spectrometry (*SI Appendix*, Fig. S1 *A* and *B*). The peptide composition, spectroscopic properties, and pigment compositions of them are shown in *SI Appendix*, Fig. S1 *B*–*E*. It is observed that the PsaA/B subunits of PSI–AcpPCI samples from *A. carterae* and *Symbiodinium* are remarkably smaller compared to those in a centric diatom *Chaetoceros gracilis* (Cg) (*SI Appendix*, Fig. S1*B*).

Two main particles were observed during 3D classification of the Ss-PSI–AcpPCI sample; thus, three structures of PSI–AcpPCI from these two dinoflagellates were determined by cryo-EM with overall resolutions of 2.90, 2.99, and 2.70 Å based on the "gold standard" of Fourier shell correlation (FSC) = 0.143 (*SI Appendix*, Fig. S2 *A* and *B* and Table S1). The monomeric Ac-PSI–AcpPCI is the largest particle, which is composed of PsaA/B/C/D/E/F/I/J/L/M/R subunits as the PSI core and 18 AcpPCI antennae distributed into two layers (Fig. 1 *A*–*C* and *SI Appendix*, Table S2). Among the AcpPCI subunits, 11 are located in an inner layer encircling the core, and seven forms a discontinuous second layer (Fig. 1*C*). Ac-AcpPCI-12/13 bind to the PsaD/L side through inner Ac-AcpPCI-2/3/4 subunits, and Ac-AcpPCI-14/15/16/17/18 bind to the PsaJ/F side by inner Ac-AcpPCI-5/6/7/8 subunits (Fig. 1*A*). No water-soluble PCP antennae were found associated with the Ac-PSI–AcpPCI supercomplex. In addition to the protein subunits, 223 Chls *a*, 39 Chls *c*, 49 Pers, 49 Ddxs, 12 dinoxanthins (Dins), 12 β-carotenes (Bcrs), as well as several electron transfer cofactors and lipids (*SI Appendix*, Fig. S2*C* and Table S2) were identified in Ac-PSI–AcpPCI. This results in a supercomplex consisting of 29 subunits and more than 411 cofactors, with an overall molecular weight of 0.89 MDa.

The two coral symbiotic Ss-PSI–AcpPCI supercomplexes have a similar composition of the PSI core as that of Ac-PSI–AcpPCI with 11 PSI core subunits and two additional unknown subunits but differ in the number of AcpPCI antennae (Fig. 1 *D* and *E*). One Ss-PSI–AcpPCI supercomplex contains 12 antennae, whereas the other one has 14 antennae identified by the 3D classifications (Fig. 1*F* and *SI Appendix*, Fig. S2*B*). The different number of antennae in the two Ss-PSI–AcpPCI structures suggests that some weakly bound AcpPCI subunits have been lost during the preparation process due to their sensitivity to detergent. Superimposition of the two PSI–AcpPCI clearly showed that except the 2 additional core subunits and 4 changed peripheral AcpPCI antennae present in *Symbiodinium*, the symbiotic Ss-PSI–AcpPCI supercomplex exhibits similar assemblies to that of Ac-PSI–AcpPCI (*SI Appendix*, Fig. S3*A*).

Structure of the Dinoflagellate PSI Core. The Ac-PSI core contains eight transmembrane subunits (PsaA/B/F/I/J/L/M/R) and three extrinsic subunits (PsaC/D/E) located at the stromal side (Figs. 1 *A* and *B* and 2*A*), whereas Ss-PSI core contains, in addition to these subunits, two additional core subunits, Unk1 at the stromal surface and Unk2 at the lumenal surface (Fig. 1 *D* and *E* and *SI Appendix*, Fig. S4 *D* and *E*). Similar to the diatoms PSI cores, the dinoflagellate PSI core also lacks the PsaG/H/K/N/O subunits that are otherwise present in green algae and higher plants (6–13). Thus, the assembly of their peripheral antennae differs from that in photosynthetic organisms of the green lineage (*SI Appendix*, Fig. S3 *E* and *F*). On the other hand, the dinoflagellates PSI core lacks PsaS, which is unique in diatoms (Fig. 1 *B* and *E* and *SI Appendix*, Table S2). Furthermore, the sequences of many PSI core subunits of *A. carterae* and *Symbiodinium* show significant divergence (*SI Appendix*, Fig. S1*B* and Table S2), resulting in notable variations in their lengths and structures (Fig. 2 *B* and *D* and *SI Appendix*, Figs. S4 *A* and *C* and S5 and Table S3). The major PsaA/B subunits of *A. carterae* PSI exhibit distinctive characteristics with a reduction of around 96 and 114 residues (*SI Appendix*, Fig. S5 *A* and *B*), compared to those in the PSI structures from *C. gracilis* and other species. The PsaA and PsaB subunits of *A. carterae* have 11 strictly conserved transmembrane helices, but they have many shorter loop regions (Fig.2*B* and *SI Appendix*, Fig. S5 *A* and *B*), making them shorter than those of the other organisms. The variable regions of Ac-PsaA/B are observed in the loop regions from N terminus to helix-8, while the length from helix-8 to C terminus is almost identical to that of *C. gracilis* (*SI Appendix*, Fig. S5 *A* and *B*).

The loop-3/4 (between helices-3/4) and loop-7/8 of Ac-PsaA at the lumenal surface, as well as the N-terminal loop and loop-4/5 at the stromal surface, are found to be shorter by around 20 amino acids (Fig. 2*B* and *SI Appendix*, Fig. S5*A*). In addition, loop-1/2 and loop-6/7 at the stromal surface have an absence of 5–8 amino acids compared to the PsaA subunit in *C. gracilis* (Fig. 2*B* and *SI Appendix*, Fig. S5*A*). As a result, the Ac-PsaA is shorter by 96 residues in comparison with the corresponding PsaA sequence from *C. gracilis* (Fig. 2*B* and *SI Appendix*, Fig. S5*A*). Similar absences of residues from the N terminus to helix-8 and some variations in the loop regions lead to a substantial shortening of 114 residues in Ac-PsaB (Fig. 2*B* and *SI Appendix*, Fig. S5*B*). The shortened loops of Ac-PsaA/B result in the lack of a remarkable number of Chl *a* and Car sites (Fig. 2*C*), which have not been observed in other photosynthetic species. PsaA and PsaB in *A. carterae* have 6 and 8 fewer Chl *a* sites than those of *C. gracilis* due to the absence of amino acid residues in the loop structures

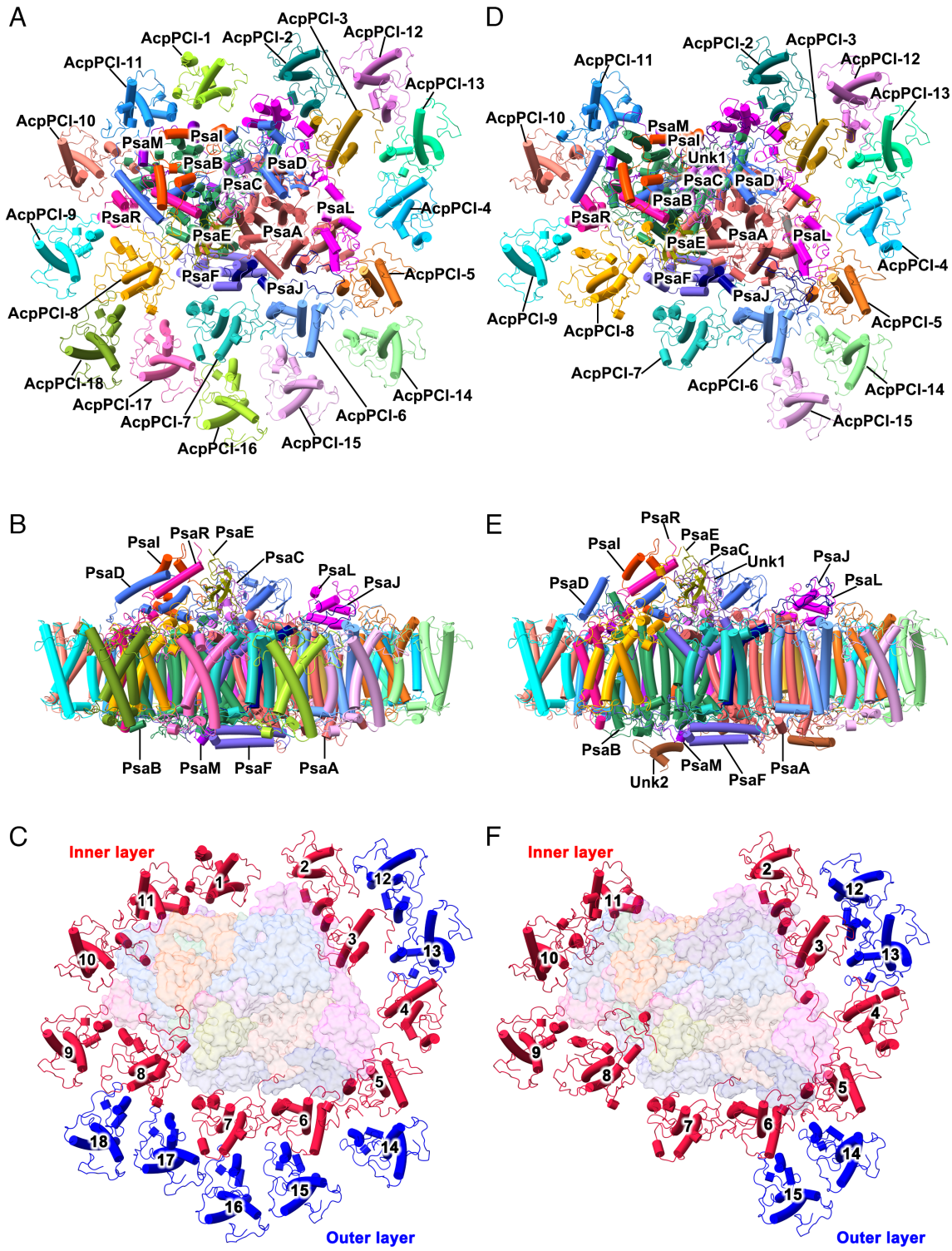

Fig. 1. Overall structures of PSI-AcpPCI supercomplex from *A. carterae* (*Left*) and *Symbiodinium* (*Right*). (*A*) Top view of Ac-PSI–AcpPCI supercomplex from the stromal side. (*B*) Side view of Ac-PSI–AcpPCI supercomplex. (*C*) Two AcpPCI antennae layers surrounding the PSI core in Ac-PSI–AcpPCI supercomplex. (*D-F*) Detailed subunits of Ss-PSI–AcpPCI supercomplex from the top and side views. In (*A*), (*B*), (*D*), and (*E*), protein subunits are shown as cylindrical cartoons and colored individually as indicated. In (*C*) and (*F*), AcpPCIs in the inner layer and the outer layer are indicated by red and blue cartoons, respectively.

at the stromal side (Fig. 2*C*). At the lumenal side, 4 and 3 Chls *a* in PsaA and PsaB of *C. gracilis* were not found in *A. carterae*. However, Ac-PsaA developed an additional Chl *a* 855 and Ac-PsaB developed an additional Chl *a* 854 (Fig. 2*C*). As a result of these differences, the Ac-PsaA/B subunits bind only 36 and 30 Chls *a*, thus there is a total of 19 Chls fewer in *A. carterae* in comparison with those of *C. gracilis* PsaA/B. As shown in *SI Appendix*, Table S2, Ss-PsaA/B tends to reduce Chls and Cars by a similar amount, despite that some variations existed in the loop structures and pigment sites between the red tidal and coral symbiotic dinoflagellate PsaA/B (*SI Appendix*, Figs. S4 *A* and *B* and S5 *A* and *B*).

In contrast to PsaA/B, Ac-PsaC/E are only 4 to 9 residues longer in their N or C terminus compared to their counterparts in *C. gracilis* PSI, suggesting a high degree of conservation in both of their structures and locations (*SI Appendix*, Fig. S5 *C* and *E*). The C terminus of Ac-PsaC forms an additional hydrogen bond with

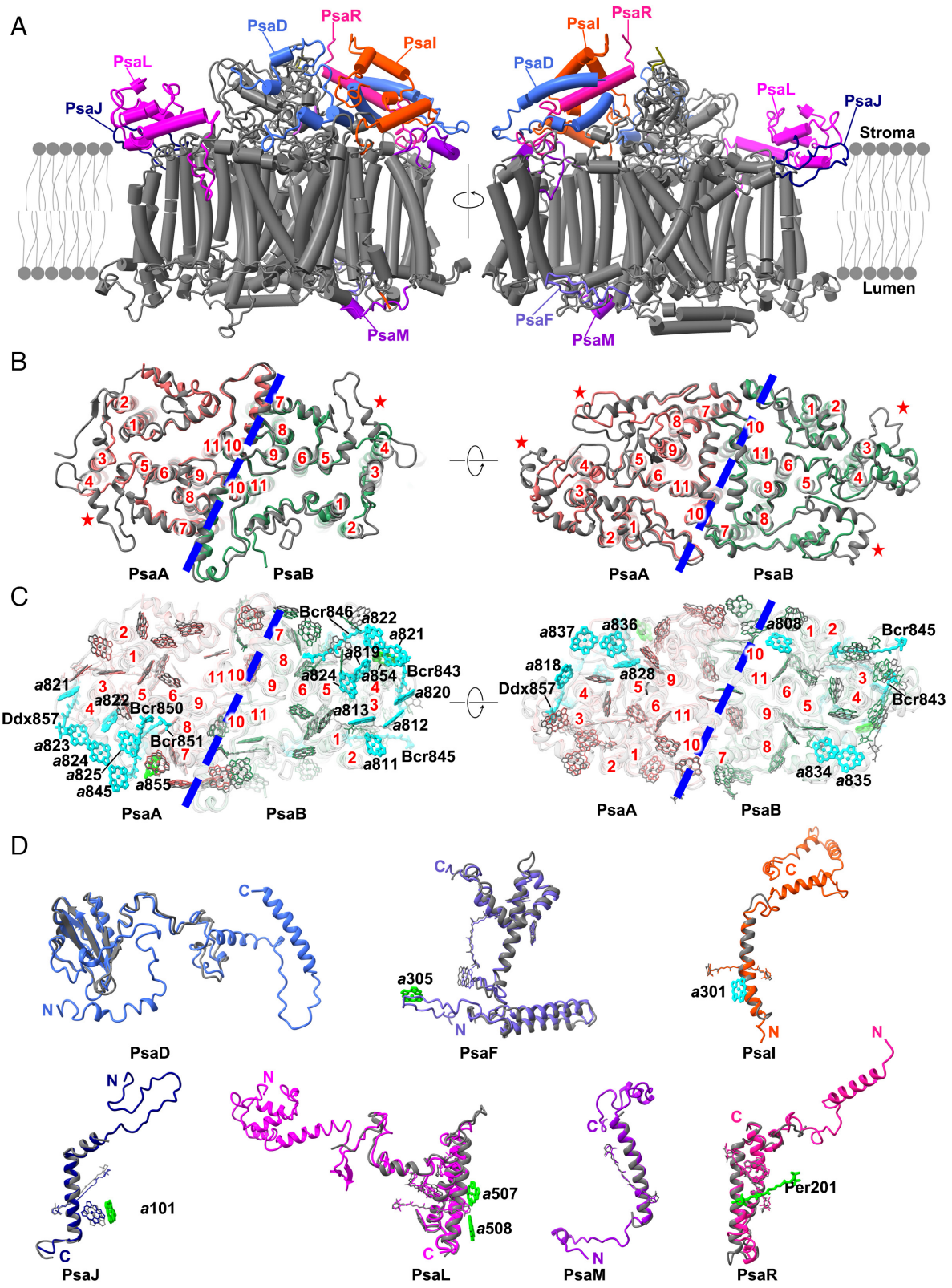

Fig. 2. Comparisons of the PSI core subunit structures between *A. carterae* and *C. gracilis*. (*A*) Conserved secondary structures of Ac-PSI core (gray) and the additional subunits of PsaD/F/I/J/L/M/R. (*B*) Different loop structures of PsaA/B between *A. carterae* (light pink/green) and *C. gracilis* (gray) at the stromal (*Left*) and lumenal (*Right*) sides, respectively. The 11 transmembrane helices of PsaA/B are labeled with red numbers, and the loop regions with significant structural differences between *A. carterae* and *C. gracilis* are labeled with red asterisks. (*C*) Comparisons of the Chl and Car sites in the PsaA/B. (*D*) Comparisons of the PsaD/F/I/J/L/M/R structures between *A. carterae* (colorful) and *C. gracilis* (gray). Conserved pigment sites are shown in sticks with the same colors as their subunits, whereas specific pigment-binding sites in *A. carterae* and *C. gracilis* PSI are indicated by green bold and cyan bold sticks, respectively.

PsaB (*SI Appendix*, Fig. S6*A*), thereby enhancing the binding of PsaC to the PSI core. The other core subunits, PsaF/I/J/L/M/R preserve all of their transmembrane helices (Fig. 2*D* and *SI Appendix*, Fig. S5 *F–K*). However, the N- or C-terminal loops of these subunits and the extrinsic subunit Ac-PsaD exhibit significant elongations than those in *C. gracilis* (Fig. 2*D* and *SI Appendix*, Fig. S5*D*).

Specifically, Ac-PsaF/J/L/R have longer N-terminal loops, Ac-PsaI displays a longer C-terminal loop, and Ac-PsaM possesses extended N- and C-terminal loop structures (Fig. 2*D*). PsaD is located adjacent to PsaC at the stromal side. In comparison to that in *C. gracilis*, Ac-PsaD has additional 60 and 66 amino acids respectively in the N- and C-terminal regions (Fig. 2*D* and *SI Appendix*, Fig. S5*D*). No additional ligands or electron accepter were identified in these two motifs of PsaD. The additional 27 residues of Ac-PsaF in the N-terminal loop facilitate the binding of an extra Chl *a*305 (Fig. 2*D* and *SI Appendix*, Fig. S5*F*), potentially enhancing its interaction with PsaB. These features are also distinctly different from those of green algae, higher plants, and red algae (*SI Appendix*, Table S3).

In previous PSI structures, the PsaI subunit consisted of a single transmembrane helix and fewer loop residues located between PsaL and PsaM (4, 5). The C-terminal loop of Ac-PsaI has an additional 88 amino acid residues in comparison with that in *C. gracilis* (Fig. 2*D* and *SI Appendix*, Fig. S5*G*). This extended loop motif consists of three short α-helices positioned on top of Ac-PsaD and Ac-PsaR at the stromal surface (Fig. 2 *A* and *D*). However, we observed that Chl *a*301 found in *C. gracilis*-PsaI (Cg-PsaI) is absent in Ac-PsaI (Fig. 2*D*). On the other hand, Ac-PsaJ has an extra 31 residues in its N-terminal region and an additional Chl *a*101 is bound in the transmembrane helix region (Fig. 2*D* and *SI Appendix*, Fig. S5*H*).

Ac-PsaL features an elongated N-terminal extension (with an additional 113 residues) including five short helices located above the loop-4/5 region of Ac-PsaA (Figs. 2*A* and 3*C* and *SI Appendix*, Fig. S5*I*). Compared with the PsaL of *C. gracilis*, two additional Chls *a*507/508 were found in proximity to the transmembrane helix region of Ac-PsaL (Fig. 2*D*). The location of Ac-PsaM is consistent with that in *C. gracilis*, featuring longer N- and C-terminal loop structures (22 and 37 residues, respectively) (Fig. 2*D* and *SI Appendix*, Fig. S5*J*). The PsaR subunit was identified in the previous PSI core of diatom and cryptophyte, as well as in the present three PSI structures of dinoflagellates. The N and C terminus of Ac-PsaR were both located at the stromal side, with an additional 44 residues in its N-terminal region compared to that in *C. gracilis* (Fig. 2*D* and *SI Appendix*, Fig. S5*K*). An additional Per201 site was found in the transmembrane helix region of Ac-PsaR (Fig. 2*D*). As a result, three additional Chls *a* and one Car were found in these minor core subunits of *A. carterae* compared to *C. gracilis*. The structures of these minor PsaD/F/I/L/K/R subunits have remarkably similar elongations in both *A. carterae* and *Symbiodinium* as well as some small variations in the N- and C-terminal structures and pigment sites (*SI Appendix*, Fig. S4*C*). These results suggest that both the Ss-PSI core and the Ac-PSI core enlarged their minor subunits to compensate for the pigment loss in the major PsaA/B subunits (Fig. 2 *B* and *C* and *SI Appendix*, Fig. S4 *A* and *B*).

Assembly Pattern of the PSI–AcpPCI Supercomplexes. The variations of PSI core subunits of *A. carterae* and *Symbiodinium* alter the interactions between PsaA/B and the minor core subunits, and therefore affects their interactions with the peripheral AcpPCI antennae. The additional N-terminal region of Ac-PsaD formed a curved loop that interacts with PsaL and subsequently interacts with PsaB/I/C (Figs. 2*A* and 3*A*). One of the helices in its elongated C-terminal loop is positioned between PsaB and the additional N-terminal motif of PsaI, whereas another helix in the extended

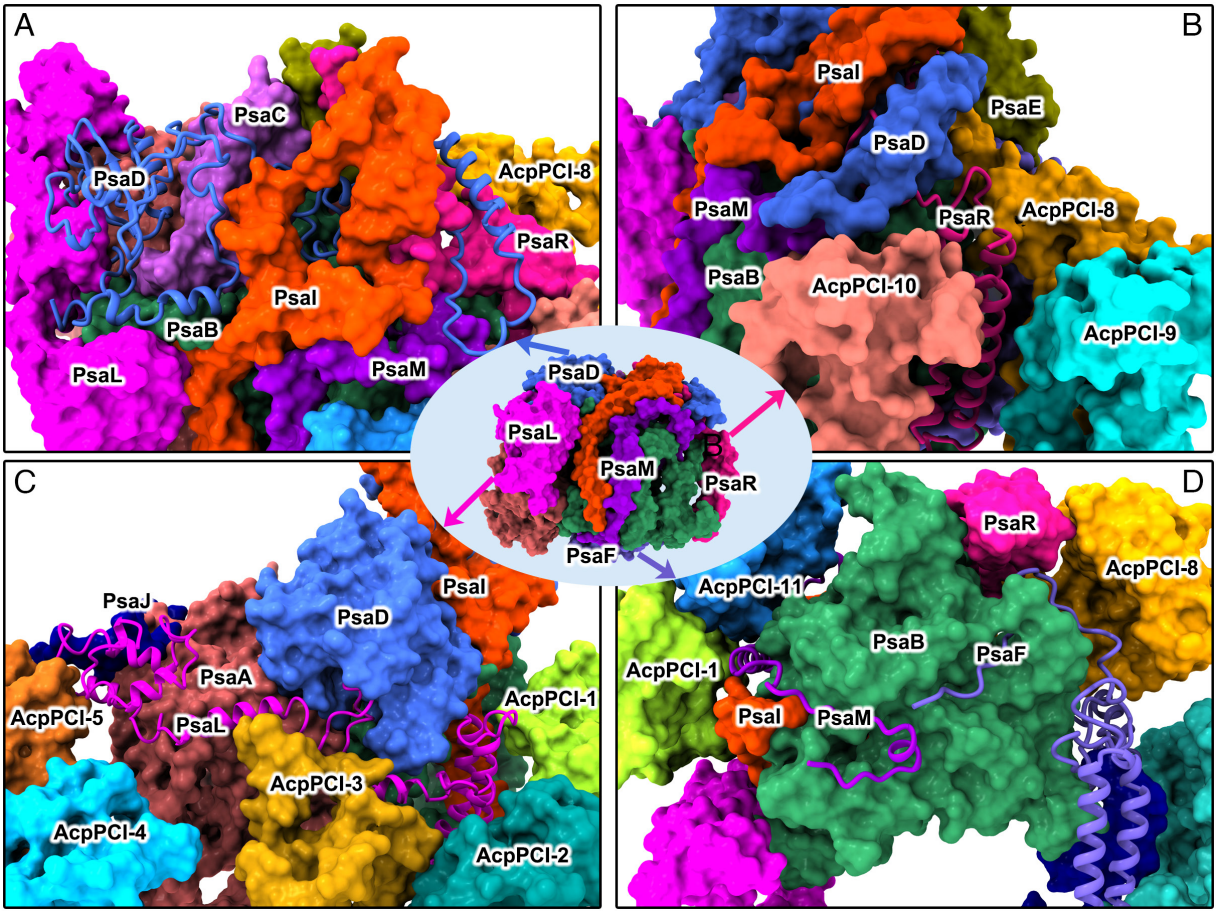

Fig. 3. Assembly and interactions of Ac-PSI core subunits. Four regions of interactions mediated mainly by PsaD (*A*), PsaR (*B*), PsaL (*C*), and PsaF/M (*D*) shown in cartoons. The color codes of subunits are the same as those in Fig. 1.

C terminus of PsaD is located on the surface of PsaM and PsaR (Figs. 2*A* and 3*A*). Ac-PsaR inserts its additional N-terminal helix into a cavity formed by the extra helices of PsaD and PsaI (Figs. 2*A* and 3*B*). The N-terminal motif of Ac-PsaI forms three helices (Fig. 2*A*) and attaches to the stromal surface to enhance the stability of PsaC/D/E (Fig. 3 *A* and *B*). Ac-PsaL acts as a bridge connecting PsaA/D/J and five antenna subunits (AcpPCIs-1/2/3/4/5) at the stromal side (Fig. 3*C*). The long N-terminal region of Ac-PsaL has a helix at the stromal surface and a coiled structure inserted into the membrane to enhance the binding between PsaL and AcpPCI-3 (Figs. 2*D* and 3*C*). Both Ac-PsaF and Ac-PsaM extend their N-terminal loops primarily at the lumenal surface of PsaB and then connect AcpPCI-8 and AcpPCI-1 to the PSI core (Figs. 2*A* and 3*D*).

Analogous to the *C. gracilis* PSI–FCPI supercomplex (Cg-PSI–FCPI), the conserved motifs of Ac-PsaF/R play crucial roles in facilitating the attachment of peripheral antennae. Two transmembrane helices and the C-terminal loop of PsaF at the stromal surface enable the associations of Ac-AcpPCI-5/6/7 with the PSI core (Fig. 1*A*), just like the arrangement observed in Cg-PSI–FCPI (*SI Appendix*, Fig. S3*B*). Ac-PsaR also interacts with PsaB and mediates the binding of three antennae (AcpPCI-8/9/10) (Fig. 3*B*). Ac-AcpPCI-12/13 in the outer layer are attached to the Ac-AcpPCI-2/3/4 side, while Ac-AcpPCI-14/15/16/17/18 are connected to the Ac-AcpPCI-5/6/7/8 side (Fig. 1*A*). In contrast to their counterparts in Cg-FCPI, Ac-AcpPCI-7/8 have longer C- and N-terminal loop structures, which facilitate their attachment to the PSI core (Fig. 4*A* and *SI Appendix*, Fig. S7 *G* and *H*). In contrast, Ac-AcpPCI-4 has lost a portion of its C-terminal loop (Fig. 4*A* and *SI Appendix*, Fig. S7*D*) and therefore cannot interact with the PSI core subunits directly. Instead, Ac-AcpPCI-4 associates with the Ac-PSI core through the adjacent Ac-AcpPCI-3/5 antennae (Fig. 4*A*).

The assembly of the Ac-PSI–AcpPCI complex relies on numerous hydrogen bonds and hydrophobic interactions among modified PSI core subunits and AcpPCIs, similar to previously resolved PSI structures. Many hydrogen bonds between Ac-PsaB and Ac-PsaC/M/R (*SI Appendix*, Fig. S6 *A–D*), between Ac-PsaD and Ac-PsaC/R (*SI Appendix*, Fig. S6 *E–G*), between Ac-PsaI and Ac-PsaR (*SI Appendix*, Fig. S6*H*), as well as between Ac-AcpPCI-8 and Ac-PsaF/R (*SI Appendix*, Fig. S6 *I* and *J*), are primarily ascribed to the variations in the loop regions of these subunits. In addition, several lipids were identified at the interfaces between the Ac-PSI core and Ac-AcpPCIs (*SI Appendix*, Fig. S6 *J–L*), which may enhance the interactions. The organization among adjacent Ac-AcpPCIs resembles those observed among FCPIs within the Cg-PSI–FCPI supercomplex which are contributed by hydrophobic and hydrophilic interactions between proteins-proteins, proteins-pigments, and pigments-pigments (*SI Appendix*, Fig. S8). The core subunits in Ss-PSI–AcpPCI also exhibit similar modifications as observed in Ac-PSI-AcpPCI (*SI Appendix*, Fig. S4 *A* and *C*), thus *Symbiodinium* has similar changes mainly in the loop regions of Ss-AcpPCI to facilitate the interactions with the PSI core and adjacent antennae (*SI Appendix*, Fig. S4*F*).

Structures of Ac-AcpPCI Subunits and the Binding Pigments. The structures of 17 Ac-AcpPCI subunits were built based on the results of mass spectrometric and transcriptome analyses, whereas a partial sequence of Ac-AcpPCI-18 was employed for construction of Ac-AcpPCI-16 due to their similar structures in the cryo-EM map. The local maps for the peripheral AcpPCI-12/13/14 subunits exhibit poor resolution (*SI Appendix*, Fig. S2 *A* and *D*), and the most appropriate sequences were selected from the transcriptome data to fit into the density maps. The structures of helices are relatively conserved, whereas the N/C-terminal loops and other loop regions show less conservation (*SI Appendix*, Fig. S9 *A* and *B*). As a result, the peripheral Ac-AcpPCI antennae have slight positional shifts in comparison with the FCPIs in diatoms, LHCRs in red algae, and ACPIs in cryptophytes (*SI Appendix*, Fig. S3 *B–D*). Moreover, they display more remarkable shifts or completely different positions when compared to LHCIs in green algae and higher plants (*SI Appendix*, Fig. S3 *E* and *F*).

The 18 Ac-AcpPCI subunits were classified into two major groups by phylogenetic analysis, namely, an Lhcr-type and an Lhcf-type (Fig. 4*B*). The Lhcr-type antennae include Ac-AcpPCI-4/5/6/7/8/10/11 and the Lhcf-type antennae consist of Ac-AcpPCI-1/2/3/9/12/13/14/15/16/17/18. The Lhcr-type antennae are located in the inner layer, whereas the majority of Lhcf-type antennae are arranged in the outer layer. Among them, Ac-AcpPCI-7 is identified as a Lhcr1-type antenna and occupies a position similar to Cg-FCPI-7 (Fig. 4 *A* and *B* and *SI Appendix*, Fig. S3*B*), which is in close interactions with the transmembrane helices of Ac-PsaF. Ac-AcpPCI-7 possesses a long C-terminal loop that interacts with Ac-PsaJ and Ac-PsaA strongly (Figs. 4*A* and *SI Appendix*, Fig. S9*A*), thereby strengthening its association with the Ac-PSI core. Ac-AcpPCI-7 contains 11 Chl sites and 5 Ddx sites that are similar to Cg-FCPI-7 (*SI Appendix*, Table S4), the only exceptional site is the shifted location of Chl *a*405, which moves from the lumenal side to the stromal side around helix C (Fig. 4*A* and *SI Appendix*, Fig. S7*G*). The structure of Ac-AcpPCI-8 is partially similar to Cg-FCPI-8 but different from the main Lhcr groups (Fig. 4*B*). In contrast to Cg-FCPI-8, Ac-AcpPCI-8 lacks a small part of the B-C loop and gained an additional 40 residues in the N-terminal loop (*SI Appendix*, Figs. S7*H* and S9), and it interacts with PsaR on the stromal surface to enhance their association (Figs. 3*B* and 4*A*). However, Ac-AcpPCI-8 is unable to bind Chls *a*405/*a*413 found in Cg-FCPI-8 which are close to helix C, nor to Fxs 307/310 on the periphery of the protein scaffold, while the Chl *c*405 site is identified (Fig. 4*A* and *SI Appendix*, Fig. S7*H*).

Ac-AcpPCI-6/11 constitute a branch (Fig. 4*B*) within the Lhcr group but share similar protein structures with other Lhcr-type AcpPCIs except some slight differences in their loop regions (*SI Appendix*, Fig. S7 *F* and *K*). Ac-AcpPCI-6 exhibits a nearly identical structure to Cg-FCPI-6, except for the presence of Chl *a*412 near the B-C loop of Cg-FCPI-6 (*SI Appendix*, Fig. S7*F*). However, Cg-FCPI-11 belongs to another Lhcr branch which is distinct from Ac-AcpPCI-11 (Fig. 4*B*), there are more differences in their pigment binding sites (*SI Appendix*, Fig. S7*K* and Table S4). Ac-AcpPCI-4/5/10 share similar helices as that of FCPI-9 from *C. gracilis* (Fig. 4*B*). Ac-AcpPCI-4 has a shorter N-terminal loop than Cg-FCPI-4 where four Chls and three Cars found in Cg-FCPI-4 are missing (*SI Appendix*, Fig. S7*D* and Table S4). The helix D in the C-terminal region of Cg-FCPI-5 was not found in Ac-AcpPCI-5, and their loop structures and pigment sites exhibit remarkable differences (*SI Appendix*, Fig. S7*E* and Table S4). Moreover, the Lhcr-type Ac-AcpPCI-10 has the same binding sites for Chls 400–411 and 5 Car sites in the central region as Cg-FCPI-10 (*SI Appendix*, Fig. S7*J* and Table S4); however, three Chls *a*413/*a*414/*a*415 in Ac-AcpPCI-10 and Chl *a*412 in Cg-FCPI-10 are coordinated by their different C-A and B-C loops, respectively (*SI Appendix*, Fig. S7*J*).

The Lhcf-type antennae associated with the Ac-PSI core consist of Ac-AcpPCI-1/3 and Ac-AcpPCI-2/9/12/13/14/15/16/17/18; however, their structures differ from the typical dimeric Pt-Lhcf4 (Lhcf4 from *Phaeodactylum tricornutum*) and tetrameric Cg-Lhcf1 (Fig. 4*B*). The structure of Ac-AcpPCI-3 is similar to Cg-FCPI-3, with only slight differences in their loop regions and pigment binding sites (*SI Appendix*, Fig. S7*C*). Ac-AcpPCI-1 belongs to a Tp-Lhcf7 (Lhcf7 from *Thalassiosira pseudonana*) type branch

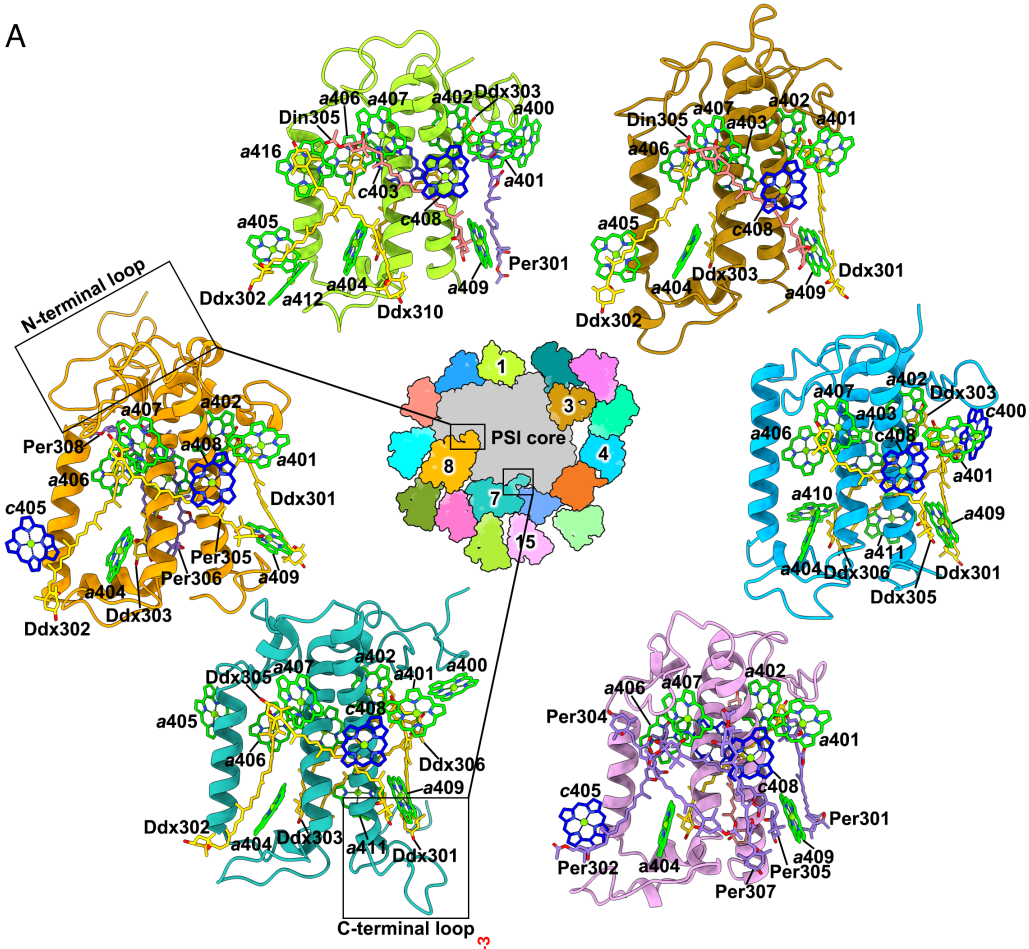

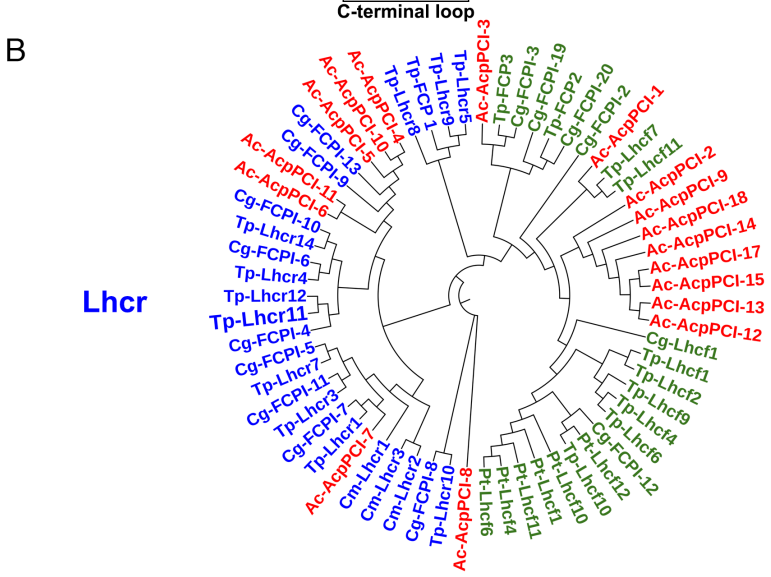

Fig. 4. The structures, locations, and phylogenetic analysis of Ac-AcpPCI antennae. (*A*) The pigment sites, secondary structures, and locations of five representative Ac-AcpPCIs (Ac-AcpPCI-1/3/4/7/8/15) around the Ac-PSI core. The Chl *a*, Chl *c*, Per, Ddx, and Din molecules are shown in green, blue, medium purple, gold, and coral sticks, respectively. (*B*) Phylogenetic tree analysis of the light-harvesting antennae from *A. carterae*, *C. merolae*, *C. gracilis*, *P. tricornutum*, and *T. pseudonana*. The groups of Lhcr and Lhcf types are labeled in blue and green, respectively, whereas the antennae of *A. carterae* are labeled in red.

(Fig. 4*B*), and their pigment binding sites including Chls 401 to 409, Cars 301 to 303, and Car 305, are highly conserved in the central region (*SI Appendix*, Fig. S10 *A* and *B* and Table S4), whereas some Chl and Car sites located in the peripheral region are different *SI Appendix*, Fig. S7*A*. In Ac-AcpPCI-13/14/15/16/17/18, nine Chls and seven Cars are tentatively assigned, whereas Ac-AcpPCI-9/12 lacks a Car306 (*SI Appendix*, Table S4). Notably, Per304 has shifted from the stromal surface to the membrane region (Fig. 4*A* and *SI Appendix*, Figs. S7*L* and S10*B*). Ac-AcpPCI-2 features a longer C-A loop region that distinctly differs from other antennae (*SI Appendix*, Fig. S9*A*) and lacks Car304 but binds specifically a Chl *a*417 and a Per309 (Fig. 4*B* and *SI Appendix*, Figs. S7*B* and S10*E*).

As shown in *SI Appendix*, Table S4, we found that the Chl binding sites within the central region of both Lhcr-type and Lhcf-type AcpPCIs are relatively conserved (*SI Appendix*, Fig. S10 *A* and *B*). The Ac-AcpPCIs are characterized by high variability in their loop regions, consequently exhibiting different binding sites for Chls *a* in their peripheral region (*SI Appendix*, Fig. S10 *A* and *B* and Table S4). The Lhcf-type Ac-AcpPCIs bind more Chls *c* through their Chl *c*403 and Chl *c*405 sites (*SI Appendix*, Fig. S10*A* and Table S4). Unlike the conserved Chl *a*400 sites in Ac-AcpPCI-6/7/11

and their Cg-FCPI counterparts, the variations in the N-terminal loops of Ac-AcpPCI-4/5/10 lead to the shifted locations of the Chl *c*400 sites, which was mainly coordinated by Ddx306 and Tyr32 (*SI Appendix*, Fig. S10 *A* and *C*). Interestingly, Chl *c*400 utilizes its polar propionic acids group to interact with the Mg atom of Chl *a*401 (*SI Appendix*, Fig. S10*C*). Chls *a*413/*a*414/*a*415 of AcpPCI-10 are bound to the C-A loop region at the interface between PsaB, mediating the excitation energy transfer (EET) from AcpPCI-10 to PsaB (Fig. 5*C* and *SI Appendix*, Fig. S7*J*). Both Chl *a*416 in Ac-AcpPCI-1 and Chl *a*417 in Ac-AcpPCI-2 bound to their C-A loop regions (*SI Appendix*, Figs. S7 *A* and *B* and S10*E*).

The 18 Ac-AcpPCIs display remarkable diversity in both the types and locations of carotenoids. In contrast to Cg-FCPIs, which bind Fx and a small amount of Ddx, Ac-AcpPCIs bind a large amount of xanthophyll cycle carotenoids (such as Ddx, Dtx, and Din) and keto-Car (Per) (*SI Appendix*, Table S2). Ac-PSI–AcpPCI has a relatively stronger ability to capture green light compared to Cg-PSI–FCPI (*SI Appendix*, Fig. S1*D*), probably because of its AcpPCIs and the Cars bound. Among the Car sites, four sites (301, 302, 303, and 305) are strictly conserved between Cg-FCPIs and Ac-AcpPCIs (*SI Appendix*, Fig. S10*B* and Table S4). All 303 sites in Ac-AcpPCI are assigned as Ddx, whereas the 305 site is a mixed site for Ddx, Per, or Din (*SI Appendix*, Fig. S10 *G* and *H* and Table S4). Per belongs to a specific class of keto-carotenoids that form a conjugated lactone. Per304 in the Lhcf-type Ac-AcpPCI antennae located in the central region of the membrane between Per302 and Per305 is remarkably different from the horizontal Fx304 on the stromal surface of Pt-Lhcf4 dimer (*SI Appendix*, Figs. S7 *I* and *L* and S10 *B* and *G*). Per302 of Ac-AcpPCI-2 forms a hydrogen bond with Phe71 (*SI Appendix*, Fig. S10*F*). In Ac-AcpPCI-9, Per304 forms hydrogen bonds with Tyr127 and Ser134/Gln135 through their conjugated carbonyl groups (*SI Appendix*, Fig. S10*G*), which may change the solvent effect of this Per and enhance their absorption of green light. In Lhcf-type Ac-AcpPCI-2/9/12~18 antennae, Cars 306/307 are coordinated to Chls *c*403/*c*408, similar to those observed in the Pt-Lhcf4 dimer (Fig. 4*A* and *SI Appendix*, Fig. S10*B* and Table S4). The absence of Car306 in Ac-AcpPCI-9/12 may be due to the tight interactions of these proteins with adjacent subunits (*SI Appendix*, Table S4). In Lhcr-type Ac-AcpPCI-4/5/6/7/10/11 antennae, Ddx306 is close to Chls 400 and the N-terminal of the antenna on the stromal side, but Car 307 is absent (Fig. 4*A* and *SI Appendix*, Fig. S10 *B* and *C* and Table S4). Two parallel Per306 and Per308 of Ac-AcpPCI-8 are located at the interface between Chl *a*403 and PsaB (Fig. 4*A* and *SI Appendix*, Fig. S9*B*), whereas Ddx308 in Ac-AcpPCI-5 is located near helix C and close to Chl *a*406 as similar as Pt-Lhcf4 (*SI Appendix*, Fig. S10*B* and Table S4). Moreover, Per309 and Ddx310 are the additional Car sites in Ac-AcpPCI-1/2 which are coordinated by the B-C loop regions and participate in the interactions among adjacent antennae (*SI Appendix*, Figs. S7 *A* and *B*, S8 *C* and *D*, and S10 *E* and *F*). All Cars in Ac-AcpPCIs are surrounded by one or more Chls, and the short distances between them ensure efficient EET as observed in Cg-FCPIs (17, 18).

Pigment Arrangement and Excitation Energy Transfer in Ac-PSI–AcpPCI. Ac-PSI–AcpPCI has Chl *a*/*c* and Chl/Car ratios of 5.71 and 2.15, respectively, which are smaller than those in Cg-PSI–FCPI (6.82 and 2.32) (*SI Appendix*, Table S2). As shown in Fig. 5, we classified the pigments of Ac-PSI–AcpPCI to reveal their arrangement and related EET pathways. Despite losing 16 Chls and 5 Cars in the PSI core (*SI Appendix*, Table S2), Ac-PSI–AcpPCI still displays a huge and well-arranged pigments network (Fig. 5 *A* and *B*). The Föster resonance energy transfer (FRET) networks obtained through computational analysis reveal variability in their favorable pathways of EET (*SI Appendix*, Fig. S11 *A* and *B* and Table S5). We divided them into the stromal and lumenal layers to analyze the pigment network and associated EET pathways (Fig. 5 *C* and *D*).

Ac-PSI–AcpPCI exhibits fewer red-shifted Chl *a*-*a* pairs for uphill energy transfer (Fig. 5 *A* and *C*), as indicated by the low-temperature fluorescence emission peak at 705 nm (*SI Appendix*, Fig. S1*E*). The red-shifted Chl *a*-*a* pairs are distributed at the interfaces between the Lhcr-type AcpPCIs and the PSI core analogous to those in Cg-PSI–FCPI (17, 18). These coupled red Chl *a*-*a* pairs provide effective energy traps to collect excitation energy from neighboring Chls, thus probably mediating the EET or serving as the quenching states among subunits. In addition, the EET pathways are also relayed by the coupled Chl *a*-*c* pairs and some crucial Chls sites distributed at the stromal and lumenal sides (Fig. 5 *C* and *D*). In the stromal layer, the Chl 403–406 pairs of Ac-AcpPCI-2/5/6/7/8/9 face to the PSI core side and directly interact with Chls of the PSI core, whereas the Chl 403–406 pairs of Ac-AcpPCI-10/11 transfer energy via a Chls *a*413/*a*414/*a*415 cluster of AcpPCI-10 to the PSI core (Fig. 5*C*). The inner Ac-AcpPCI-1/3 use individual Chl *a*400/*a*401 and Chl *a*407 to deliver energy to the PSI core (Fig. 5*C* and *SI Appendix*, Fig. S11 *C* and *D*). Due to the gap between Ac-AcpPCI-4 and the PSI core, Ac-AcpPCI-4 requires adjacent Ac-AcpPCI-3/5 to mediate energy transfer to the PSI core (Figs. 4*A* and 5*C*).

An important change observed in *A. carterae* is the appearance of the Chl *a*855 and *a*854 sites in the PsaA/B subunits (Figs. 2*C* and 5*C*), which can receive excitation energy from the peripheral antenna complexes Ac-AcpPCI-3 and Ac-AcpPCI-10 (Fig. 5*C* and *SI Appendix*, Fig. S11 *D* and *H*). Another Chl *a*305 in PsaF does not participate in energy acquisition from the peripheral antennae, but it may enhance the EET between Ac-PsaF and Ac-PsaB. An additional Chl *a*101 of Ac-PsaJ plays a role in facilitating the EET from the Ac-AcpPCI-6/7 to the PSI core (Fig. 5*D* and *SI Appendix*, Fig. S11*F*). Moreover, the identified sites Chl *a*507 and *a*508 in Ac-PsaL establish additional EET pathways with Ac-AcpPCI-1 at the stromal and lumenal sides, respectively (Fig. 5 *C* and *D* and *SI Appendix*, Fig. S11*C*). The individual Chl *a*401 in Ac-AcpPCI-6 would facilitate EET from the adjacent Ac-AcpPCI-14 (Fig. 5*C* and *SI Appendix*, Table S5). In the outer layer of Lhcf-type antennae, Ac-AcpPCI-12/13/14/15/16/17/18 employ coupled Chl *c*403–*a*406 to deliver excitation energy to the adjacent antennae in the inner layer, and an additional Chl *a*417 facilitates the EET from Ac-AcpPCI-12 to Ac-AcpPCI-2 at the stromal side (Fig. 5*C* and *SI Appendix*, Table S5).

Some EET pathways between the inner Ac-AcpPCIs to the Ac-PSI core are highly efficient due to the short distances among Chls at around 13 Å (*SI Appendix*, Table S5), such as from Chl *a*411 of Ac-AcpPCI-7 to Chl *a*101 (12.3 Å) and Chl *a*106 of Ac-PsaJ (11.3 Å) (*SI Appendix*, Fig. S11*F* and Table S5). As seen in *SI Appendix*, Table S5, several distances of EET pathways ranging from 20 to 27 Å are less efficient at both stromal and lumenal layers. Due to the change of 405 sites to Chls *c* in many Ac-AcpPCIs (Fig. 5*D*), the associated EET pathways at the lumenal layer are less efficient. Especially, Ac-AcpPCI-13 to AcpPCI-18 preferred to transfer their excitation energy via the stromal Chls layer (Fig. 5 *C* and *D*).

Discussion

After the primary endosymbiosis from cyanobacteria, oxygenic eukaryotic photoautotrophs have developed into two major lineages (28), the green lineage and the red lineage, which have diversified antenna proteins as shown in Fig. 6 and relatively conserved PSI core subunits as shown in *SI Appendix*, Fig. S12. During the evolution of oxygenic photosynthesis, these structural changes occurred

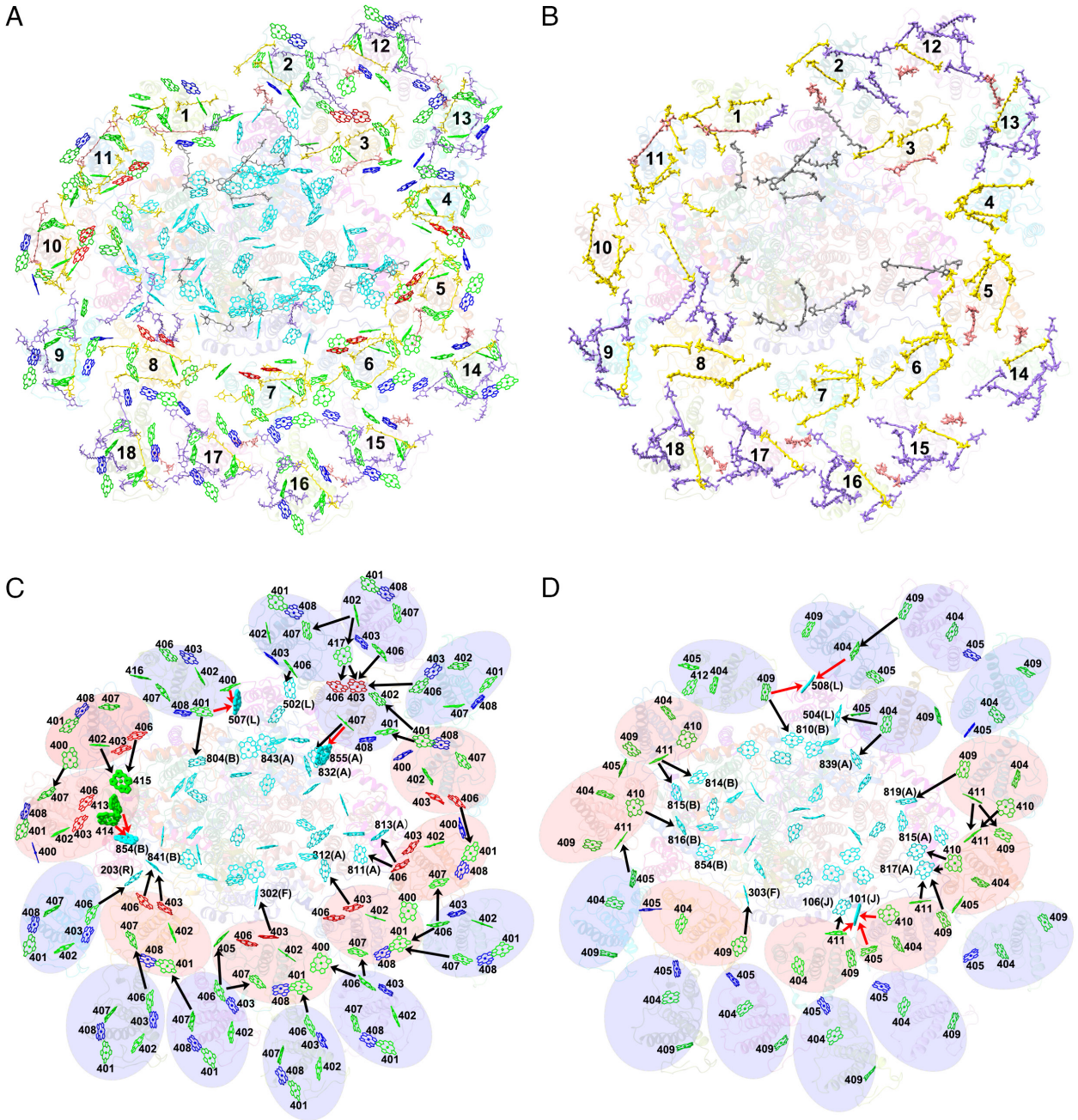

Fig. 5. Pigment arrangement and proposed EET pathways in the Ac-PSI–AcpPCI supercomplex. (*A*) Distribution of all pigments in the Ac-PSI–AcpPCI supercomplex. Chls *a* in Ac-AcpPCIs, Chls *a* in the PSI core, Chls *c*, Pers, Ddxs, Dins, and Bcrs are shown in green, cyan, blue, purple, gold, light coral, and gray sticks, respectively. Coupled Chl *a*-*a* pairs are colored in red. (*B*) Distribution of all Cars. (*C*) EET within Ac-PSI–AcpPCI at the stromal side. (*D*) EET pathways at the lumenal side. In (*C*) and (*D*), the EET pathways from outer to inner Ac-AcpPCIs and inner Ac-AcpPCIs to the PSI core are indicated by black arrows, and the additional EET pathways from inner Ac-AcpPCIs to the PSI core are indicated by red arrows. The proposed EET pathways among Chls *a* in Ac-AcpPCIs are labeled by black dashed lines. All special Chls *a* associated with EET are indicated by bold sticks.

in both the PSI core and associated light-harvesting antennae to adapt to various light environments in their habitats (23–25). The initial crucial step of these changes involves the dissociation of the PSI core trimer into monomer due to the disappearance of the C-terminal helix of PsaL (3, 4, 35–38). Although some PSI core subunits may be lost or recruited in different eukaryotic photoautotrophs, many PSI core components (PsaA/B/C/D/E/F/I/J/L) are strictly conserved in both the green and red lineages (3, 4).

The near-atomic resolution structures of PSI–AcpPCI supercomplexes solved here from a typical red tidal dinoflagellate and a coral symbiotic dinoflagellate reveal specific structural changes in many core subunits. The PsaR subunit found in diatom and cryptophyte PSIs is retained in the PSI core of *A. carterae* and *Symbiodinium*, but is absent in green algae and plants. During the endosymbiosis from red algae to diatoms and dinoflagellates, the PsaO/K disappear, whereas these two subunits are retained in the PSI of cryptophytes (17–19). Remarkable sequence and pigment changes are found in the PsaA/B/D/F/I/J/L subunits of *A. carterae* and *Symbiodinium* dinoflagellates in comparison with other organisms. For instance, the loop structures of Ac-PsaA/B are shorter by about 96/114 residues in comparison to those in diatoms and are also smaller than those of cyanobacteria, red algae, green algae, and higher plants. The PsaD/F/I/J/L subunits of *A. carterae* and *Symbiodinium* possess longer N- or C-terminal

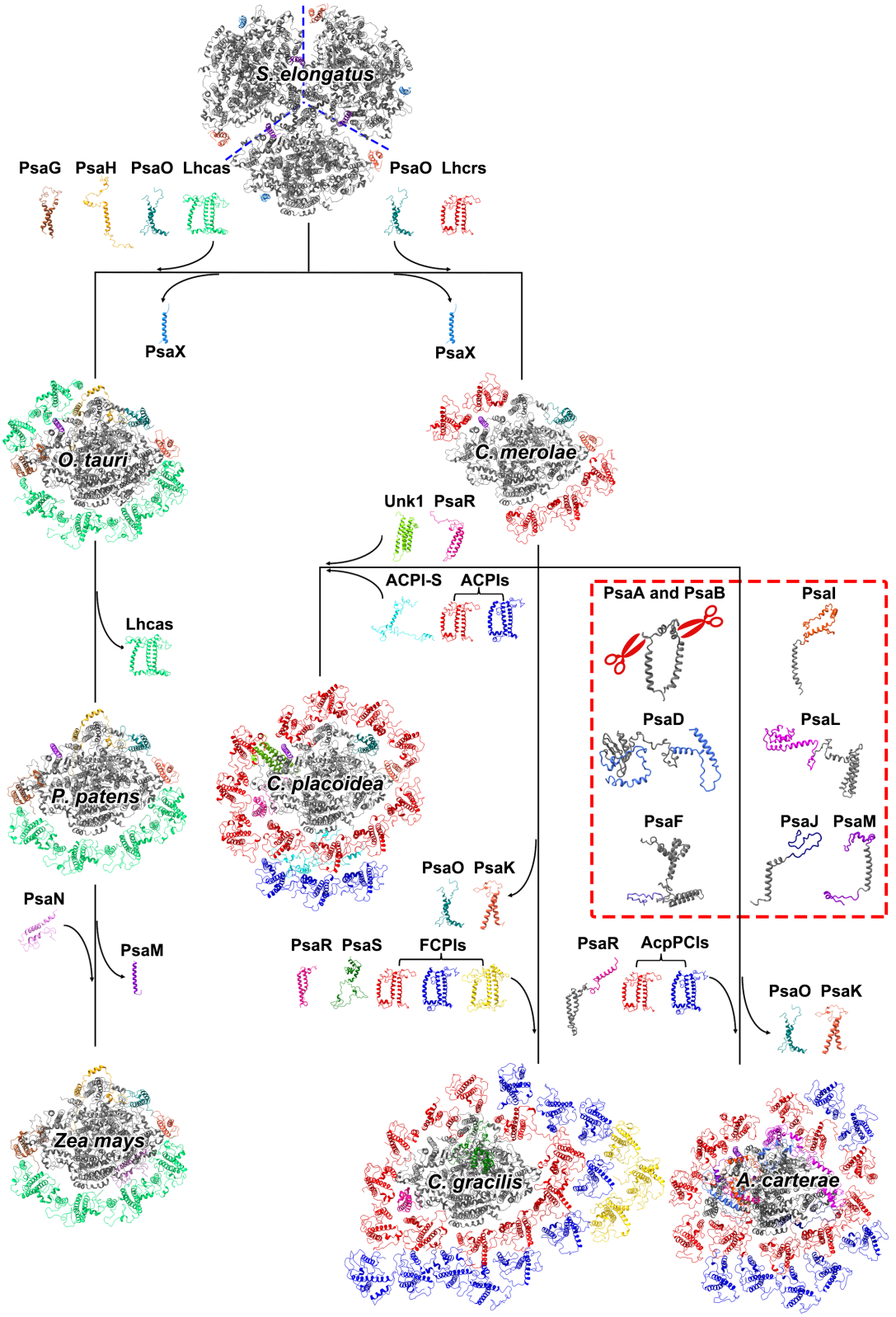

Fig. 6. Possible evolutionary changes of PSI–antennae from the cyanobacteria to the green and red lineages. PDB codes of PSI structures: PSI of a cyanobacterium (*Synechococcus elongatus*, 1JB0); PSI–LHCI of a green alga (*Ostreococcus tauri*, 7YCA), a moss (*Physcomitrium patens*, 7XQP), a higher plant (*Zea mays,* 5ZJI); PSI–LHCR of a red alga (*C. merolae*, 5ZGB); PSI–ACPI of a cryptophyte alga (*Chroomonas placoidea*, 7Y7B); PSI–FCPI of a diatom (*C. gracilis*, 6LY5); PSI–AcpPCI of a dinoflagellate (*A.carterae*, 8JW0). The evolutionary process of PSI–antennae from *C. merolae* to *A. carterae* is highlighted by the red dashed box. During this process, the PasA/B subunits have lost certain loop regions (indicated by the red scissor in the figure), while the PsaD/F/I/J/L/M subunits have gained extra secondary structure motifs and longer termini (the additional regions are colored, following the previous color).

loop regions, which compensate for the shorter PsaA/B to some extent and may provide a protective effect and maintain the stability of the PSI core. On the other hand, no extra ligands associated with the electron transfer chain are observed, suggesting that these changes in the PSI core subunits would not affect the electron transfer pathways of PSI directly.

From cyanobacteria to higher plants and diatoms, PsaA and PsaB remain plastid-encoded and display highly conserved sequences (3, 4, 38). The structures of PsaA/B in *A. carterae* and *Symbiodinium* provide the important evidence for the assembled PSI core with largely different PsaA/B sequences (Fig. 6). Although the core subunits of the anaerobic green sulfur bacterium are also relatively smaller, significant differences are found between PsaA/B in *A. carterae* and PscA-1/2 in *Chlorobaculum tepidum* (*SI Appendix*, Fig. S12) (39). These changes in the PSI core subunits of the eukaryotic dinoflagellates may be related to changes in the chloroplast genome during secondary endosymbiosis.

In higher plants and algae, numerous genes acquired from cyanobacteria have been transferred to the nucleus (40, 41). The remaining crucial genes in typical plants constitute a circular chloroplast genome which includes around 120 genes encoding subunits of PSI and PSII, cytochrome b_6f complex, ATP synthase, as well as rRNAs and a few tRNAs (42, 43). However, the conventional circular chloroplast genome is not present in dinoflagellates. Many small plasmids called "minicircles" in the plastid of dinoflagellates are recombined to give rise to fewer genes (44–48). PsaA and PsaB of dinoflagellates are proposed to be located in different minicircles with smaller lengths of around 2.2 to 3.1 kbp (45). Therefore, gene sequence deletions of the major PsaA/B genes and extensions of minor PsaD/F/I/J/L/M/R genes may occur in dinoflagellates to accommodate the changes in their specific chloroplast genome. However, these variations of PSI subunits mainly correspond to hydrophilic loops of the proteins and do not interfere with the essential photosynthetic functions (45, 46).

The 18 AcpPCIs in the periphery of the Ac-PSI core are identified as the Lhcr-type and Lhcf- type antennae, indicating that the red tidal dinoflagellate *A. carterae* deviates from endosymbiosis of a single parasite of the red lineage. These 18 AcpPCIs exhibit some remarkably conserved protein structures and pigment sites, similar to the peripheral antennae of diatoms and cryptophytes PSI (17–19). The inner antenna ring immediately surrounding the PSI core of these three algae is all composed of 11 Lhc-type antennae (18, 19), while there are distinct differences in the number and types of LHC antennae in the outer layers, which may be related to variations of the antenna structures and their binding affinity. Compared to the dominant Lhcr-type antennae in cryptophytes, diatoms, and dinoflagellates possess several Lhcf-type antennae and bind more Cars. Additionally, both dinoflagellates and cryptophytes have water-soluble light-harvesting antennae, such as PCP and phycobiliproteins (4, 19, 34), but there is no biological evidence demonstrating the PCP binding to PSI. The 18 AcpPCIs in *A. carterae* and their corresponding subunits in *Symbiodinium* exhibit variations in the structures of the loop regions and pigment binding sites, which also slightly alter the locations of each subunit compared to those in Cg-FCPIs. The core subunits and antennae of PSI–AcpPCI have evolved some extra Chl sites, which would facilitate the efficient EET to the reaction center. Therefore, the loss of several Chls would not largely affect the efficiency of EET in Ac-PSI–AcpPCI and Ss-PSI–AcpPCI supercomplexes.

Dinoflagellates employ Per to capture the blue-green light (470 to 550 nm) (32–34) and thus enhance their light-harvesting capacity in the aqueous environment. A remarkable feature of AcpPCI is that the amount of Ddx and Din is higher than Per, which differs from the dominant amount of Fx in diatom FCPI antennae (*SI Appendix*, Table S2). Therefore, dinoflagellates require water-soluble PCP antennae to capture more green light to support the PSI core under deep water. In addition, the xanthophyll cycle Cars in AcpPCIs may serve as potential quenching sites for dissipating excess excitation energy, ensuring a high capacity for photoprotection of PSI–AcpPCI to cope with strong light stress.

In summary, the dinoflagellates PSI–AcpPCI supercomplexes solved in this study exhibit some distinct features in terms of its subunit composition, loop structures, and pigments composition compared to those in red and green lineage organisms. In particular, the PSI core subunits have largely different structures and pigment binding sites compared with other PSI structures solved so far. These results reveal a unique assembly of the PSI core with its antennae, an expanded cross-section for light harvesting and an organization of an efficient network for energy transfer. Thus, the dinoflagellates PSI–AcpPCI structures provide us with valuable insights into the EET and quenching mechanisms of the PSI supercomplex as well as the changes of the peripheral antennae during evolution.

Materials and Methods

In brief, the Cells of *A. carterae* (CCMA-279) were obtained from the Center for Collections of Marine Algae at Xiamen, China. The coral symbiotic *Symbiodinium* sp. was purchased from Shanghai Guangyu Biological Technology Co., Ltd. (https://www.leadingtec.cn/product/gy-h50), and it was isolated from symbiotic coral host living in the Zhoushan region of the East China Sea. Both dinoflagellate cells were cultured in F/2 medium with artificial seawater bubbled with air, under light illumination of 40 μmol photon m^{-2} s^{-1} with a 14-h light/8-h dark cycle at 23 °C. The PSI–AcpPCI supercomplexes were isolated from the thylakoid membranes by sucrose density gradient centrifugations (*SI Appendix*, Fig. S1A), which were further purified by gel filtration (*SI Appendix*, Fig. S1C). Two PSI–AcpPCI samples were collected for cryo-EM studies (*SI Appendix*, Fig. S2A), and one Ac-PSI–AcpPCI structure was solved at a resolution of 2.90 Å and two Ss-PSI–AcpPCI structures were solved at the resolutions of 2.99 Å and 2.70 Å. All the detailed procedures including cell culture, PSI–AcpPCI purification and identification, cryo-EM images collection and structural analyses were described in *SI Appendix*, *Materials and Methods*.

Data, Materials, and Software Availability. The cryo-EM map and atomic models of Ac-PSI-AcpPCI structure at 2.90 Å resolution, and the cryo-EM map and atomic models of Ss-PSI–AcpPCI structures at 2.99 Å resolution and 2.79 Å resolution, have been deposited in the Electron Microscopy Data Bank (https://www.ebi.ac.uk/pdbe/emdb) and the Protein Data Bank (https://www.wwpdb.org) under the accession numbers of EMDB ID code 36678 (49) and PDB ID code 8JW0 (50), EMDB ID code 36742 (51) and PDB ID code 8JZE (52), EMDB ID code 36743 (53) and PDB ID code 8JZF (54), respectively. All other data are included in the manuscript and *SI Appendix*.

ACKNOWLEDGMENTS. The cryo-EM data of Ac-PSI–AcpPCI were collected at the cryo-EM system of the National Center for Protein Science, Shanghai Advanced Research Institute. The cryo-EM data of Ss-PSI–AcpPCI were collected at Beijing National Laboratory for Condensed Matter Physics, Institute of Physics, Chinese Academy of Science, and Beijing Branch of Songshan Lake Laboratory for Materials Science. We thank W.J. Zhang at the Cryo-EM Center, Institute of Genetics and Developmental Biology, Chinese Academy of Sciences for her help in data collection. This work was supported by the National Key R&D Program of China (2021YFA1300403 and 2019YFA0906300), the Youth Innovation Promotion Association of CAS (2020081), the CAS Interdisciplinary Innovation Team (JCTD-2020-06), the CAS Project for Young Scientists in Basic Research (YSBR-093), the National Natural Science Foundation of China (32222007), the Innovation Platform for Academicians of Hainan Province (2022YSCXTD0005), and the Science & Technology Specific Project in Agricultural High-tech Industrial Demonstration Area of the Yellow River Delta (2022SZX12).

Author affiliations: [a]Photosynthesis Research Center, Key Laboratory of Photobiology, Institute of Botany, Chinese Academy of Sciences, Beijing 100093, China; [b]College of Life Sciences, University of Chinese Academy of Science, Beijing 100049, China; [c]National Facility for Protein Science in Shanghai, Chinese Academy of Sciences, Shanghai 201204, China; [d]Department of Mechanical Engineering, Tsinghua University, Beijing 100084, China; [e]Laboratory for Ecology of Tropical Islands, Ministry of Education, College of Life Sciences, Hainan Normal University, Haikou 571158, China; [f]China National Botanical Garden, Beijing 100093, China; [g]Key Laboratory of Plant Resources Conservation and Germplasm Innovation in Mountainous Region, Ministry of Education, College of Life Sciences, Guizhou University, Guiyang 550025, China; and [h]Research Institute for Interdisciplinary Science, Graduate School of Natural Science and Technology, Okayama University, Okayama 700-8530, Japan

1. N. Nelson, W. Junge, Structure and energy transfer in photosystems of oxygenic photosynthesis. *Annu. Rev. Biochem.* **84**, 659–683 (2015).
2. G. D. Scholes *et al.*, Lessons from nature about solar light harvesting. *Nat. Chem.* **3**, 763–774 (2011).
3. A. Busch, M. Hippler, The structure and function of eukaryotic photosystem I. *Biochim. Biophys. Acta* **1807**, 864–877 (2011).
4. M. Suga, J.-R. Shen, Structural variations of photosystem I–antenna supercomplex in response to adaptations to different light environments. *Curr. Opin. Struct. Biol.* **63**, 10–17 (2020).
5. X. Qin *et al.*, Structure of a green algal photosystem I in complex with a large number of light-harvesting complex I subunits. *Nat. Plants* **5**, 263–272 (2019).
6. X. Qin, M. Suga, T. Kuang, J.-R. Shen, Structural basis for energy transfer pathways in the plant PSI-LHCI supercomplex. *Science* **348**, 989–995 (2015).
7. Y. Mazor, A. Borovikova, I. Caspy, N. Nelson, Structure of the plant photosystem I supercomplex at 2.6 Å resolution. *Nat. Plants* **3**, 17014 (2017).
8. J. Wang *et al.*, Structure of plant photosystem I–light harvesting complex I supercomplex at 2.4 Å resolution. *J. Integr. Plant. Biol.* **63**, 1367–1381 (2021).
9. X. Su *et al.*, Antenna arrangement and energy transfer pathways of a green algal photosystem-I-LHCI supercomplex. *Nat. Plants* **5**, 273–281 (2019).
10. M. Suga *et al.*, Structure of the green algal photosystem I supercomplex with a decameric light-harvesting complex I. *Nat. Plants* **5**, 626–636 (2019).
11. A. Ishii *et al.*, The photosystem I supercomplex from a primordial green alga Ostreococcus tauri harbors three light-harvesting complex trimers. *eLife* **12**, e84488 (2023).
12. M. Iwai, P. Grob, A. T. Iavarone, E. Nogales, K. K. Niyogi, A unique supramolecular organization of photosystem I in the moss *Physcomitrella patens*. *Nat. Plants* **4**, 904–905 (2018).
13. S. Zhang *et al.*, Structural insights into a unique PSI-LHCI-LHCII-Lhcb9 supercomplex from moss *Physcomitrium patens*. *Nat. Plants* **9**, 832–846 (2023).
14. X. Pi *et al.*, Unique organization of photosystem I–light-harvesting supercomplex revealed by cryo-EM from a red alga. *Proc. Natl. Acad. Sci. U.S.A.* **115**, 4423–4428 (2018).
15. M. Antoshvili, I. Caspy, M. Hippler, N. Nelson, Structure and function of photosystem I in *Cyanidioschyzon merolae*. *Photosynth. Res.* **139**, 499–508 (2019).
16. Y. Lu *et al.*, Role of an ancient light-harvesting protein of PSI in light absorption and photoprotection. *Nat Commun.* **12**, 679 (2021).
17. C. Xu *et al.*, Structural basis for energy transfer in a huge diatom PSI-FCPI supercomplex. *Nat. Commun.* **11**, 5081–5092 (2020).
18. R. Nagao *et al.*, Structural basis for assembly and function of a diatom photosystem I-light-harvesting supercomplex. *Nat. Commun.* **11**, 2481 (2020).
19. L.-S. Zhao *et al.*, Structural basis and evolution of the photosystem I-light-harvesting supercomplex of cryptophyte algae. *Plant Cell* **35**, 2449–2463 (2023).
20. T. Veith, C. Büchel, The monomeric photosystem I-complex of the diatom *Phaeodactylum tricornutum* binds specific fucoxanthin chlorophyll proteins (FCPs) as light-harvesting complexes. *Biochim. Biophys. Acta* **1767**, 1428–1435 (2007).
21. D. G. Durnford, R. Aebersold, B. R. Green, The fucoxanthin-chlorophyll proteins from a chromophyte alga are part of a large multigene family: Structural and evolutionary relationships to other light harvesting antennae. *Mol. Gen. Genet* **253**, 377–386 (1996).
22. W. Wang *et al.*, Structural basis for blue-green light harvesting and energy dissipation in diatoms. *Science* **363**, eaav0365 (2019).
23. C. Büchel, Evolution and function of light harvesting proteins. *J. Plant Physiol.* **172**, 62–75 (2015).
24. G. E. Hoffman, M. V. Sanchez Puerta, C. F. Delwiche, Evolution of light harvesting complex proteins from Chl *c*-containing algae. *BMC Evol. Biol.* **11**, 101 (2011).
25. P. G. Falkowski, Y. B. Chen, "In light-harvesting antennas in photosynthesis" in *Advances in Photosynthesis and Respiration*, B. Green, W. W. Parson, Eds. (Kluwer Academic Publishers, 2003), pp. 423–447.
26. C. B. Field, M. J. Behrenfeld, J. T. Randerson, P. Falkowski, Primary production of the biosphere: Integrating terrestrial and oceanic components. *Science* **281**, 237–240 (1998).
27. C. de Vargas *et al.*, Eukaryotic plankton diversity in the sunlit ocean. *Science* **348**, 1261605 (2015).
28. P. G. Falkowski *et al.*, The evolution of modern eukaryotic phytoplankton. *Science* **305**, 354–360 (2004).
29. E. J. Yang, J. K. Choi, J. H. Hyun, Distribution and structure of heterotrophic protist communities in the northeast equatorial Pacific Ocean. *Mar. Biol.* **146**, 1–15 (2004).
30. J. P. Bujak, G. L. Williams, The evolution of dinoflagellates. *Can. J. Botany* **59**, 2077–2087 (1980).
31. D. M. Niedzwiedzki, J. Jiang, C. S. Lo, R. E. Blankenship, Spectroscopic properties of the Chlorophyll *a*-Chlorophyll c_2-Perindinin-Protein-Complex (acpPC) from the coral symbiotic dinoflagellate *Symbiodinium*. *Photosynth. Res.* **120**, 125–139 (2014).
32. R. G. Hiller, P. M. Wrench, F. P. Sharples, The light-harvesting chlorophyll *a*-*c*-binding protein of dinoflagellates: A putative polyprotein. *FEBS Lett.* **363**, 175–178 (1995).
33. R. G. Hiller *et al.*, The major intrinsic light-harvesting protein of *Amphidinium*: Characterization and relation to other light-harvesting protein. *Photochem. Photobiol.* **57**, 125–131 (1993).
34. E. Hofmann *et al.*, Structure basis of light harvesting by carotenoids: Peridinin –Chlorophyll-Protein from *Amphidinium carterae*. *Science* **272**, 1788–1791 (1996).
35. P. Jordan *et al.*, Three-dimensional structure of cyanobacterial photosystem I at 2.5 angstrom resolution. *Nature* **411**, 909–917 (2001).
36. L. Zheng *et al.*, Structural and functional insights into the tetrameric photosystem I from heterocyst-forming cyanobacteria. *Nat. Plants* **5**, 1087–1097 (2019).
37. K. Kato *et al.*, Structure of a cyanobacterial photosystem I tetramer revealed by cryo-electron microscopy. *Nat. Commun.* **10**, 4929 (2019).
38. H. V. Scheller *et al.*, Role of subunits in eukaryotic Photosystem I. *Biochim. Biophys. Acta* **1507**, 41–60 (2001).
39. J.-H. Chen *et al.*, Architecture of the photosynthetic complex from a green sulfur bacterium. *Science* **370**, eabb6350 (2020).
40. W. Martin *et al.*, Gene transfer to the nucleus and the evolution of chloroplasts. *Nature* **393**, 162–165 (1998).
41. H. L. Race, R. G. Herrmann, W. Martin, Why have organelles retained genomes? *Trends Genet.* **15**, 364–370 (1999).
42. J. De Las Rivas, J. J. Lozano, A. R. Ortiz, Comparative analysis of chloroplast genomes: Functional annotation, genome-based phylogeny, and deduced evolutionary patterns. *Genome Res.* **12**, 567–583 (2002).
43. V. L. Koumandou, R. E. Nisbet, A. C. Barbrook, C. J. Howe, Dinoflagellate chloroplasts–where have all the genes gone? *Trends Genet.* **20**, 261–267 (2004).
44. Z. Zhang, B. R. Green, T. Cavalier-Smith, Single gene circles in dinoflagellate chloroplast genomes. *Nature* **400**, 155–159 (1999).
45. C. J. Howe, R. E. Nisbet, A. C. Barbrook, The remarkable chloroplast genome of dinoflagellates. *J. Exp. Bot.* **59**, 1035–1045 (2008).
46. A. C. Barbrook, C. J. Howe, Minicircular plastid DNA in the dinoflagellate *Amphidinium operculatum*. *Mol. Gen. Genet.* **263**, 152–158 (2000).
47. J. H. Wisecaver, J. D. Hackett, Dinoflagellate genome evolution. *Annu. Rev. Microbiol.* **65**, 369–387 (2011).
48. H. S. Yoon, J. D. Hackett, D. Bhattacharya, A single origin of the peridinin- and fucoxanthin-containing plastids in dinoflagellates through tertiary endosymbiosis. *Proc. Natl. Acad. Sci. U.S.A.* **99**, 11724–11729 (2002).
49. Z. Li, X. Li, W. Wang, PSI–AcpPCI supercomplex from *Amphidinium carterae*. EMDB. https://www.ebi.ac.uk/emdb/EMD-36678. Deposited 28 June 2023.
50. Z. Li, X. Li, W. Wang, PSI–AcpPCI supercomplex from *Amphidinium carterae*. PDB. http://www.rcsb.org/structure/unreleased/8JW0. Deposited 28 June 2023.
51. Z. Li, X. Li, W. Wang, PSI–AcpPCI supercomplex from *Symbiodinium*. EMDB. https://www.ebi.ac.uk/emdb/EMD-36742. Deposited 5 July 2023.
52. Z. Li, X. Li, W. Wang, PSI–AcpPCI supercomplex from *Symbiodinium*. PDB. http://www.rcsb.org/structure/unreleased/8JZE. Deposited 5 July 2023.
53. Z. Li, X. Li, W. Wang, PSI–AcpPCI supercomplex from *Symbiodinium*. EMDB. https://www.ebi.ac.uk/emdb/EMD-36743. Deposited 5 July 2023.
54. Z. Li, X. Li, W. Wang, PSI–AcpPCI supercomplex from *Symbiodinium*. PDB. http://www.rcsb.org/structure/unreleased/8JZF. Deposited 5 July 2023.